Elastoplastic-damaged meso-scale modelling of concrete with recycled aggregates

G. Mazzucco[a], G. Xotta[a], B. Pomaro[a], V.A. Salomoni[a,b,*], F. Faleschini[a]

[a] Department of Civil, Environmental and Architectural Engineering (DICEA), University of Padova, Via F. Marzolo 9, 35131 Padova, Italy
[b] Department of Management and Engineering (DTG), University of Padova, Stradella S. Nicola 3, 36100 Vicenza, Italy

ARTICLE INFO

ABSTRACT

The use of recycled concrete aggregates is very attractive from the point of view of reducing concrete production costs and of sustainability. A peculiar origin of such aggregates is that of demolitions of pre-existing concrete buildings.

Scope of this work is to analyse the challenging aspects of recycled aggregates modelling in concrete mixtures and to define a procedure to cope with them.

Particularly, numerical analyses dealing with the mechanical behaviour of concrete mixtures made of natural and recycled aggregates are here performed at the meso-scale level, distinguishing between concrete paste and aggregates themselves.

Some compelling issues for the modelling phase are addressed, i.e.: i) the correct reproduction of recycled aggregates within the concrete samples, which involves both the acquisition of the external geometry of the aggregates and their random disposition in the sample, ii) the characterization of the mechanical constitutive law of the composite.

An elastic-plastic-damaged formulation is adopted for representing the constitutive behaviour of mortar and cement matrix; the procedure is calibrated and validated so proving its predictability features when describing damage triggering and spreading within concrete samples subjected to compressive loads.

1. Introduction

According to Eurostat [1] nearly one eighth of the total waste generated in the European Union in 2012 was covered by construction and demolition wastes (C&DW), that is 320 million tons, or 636 kg per capita. It is estimated that, in the same year, 41 million tons of C&DW reached landfill and almost 18 million tons were object of recovery (i.e. backfilling). It becomes clear that wastes from construction and demolition activities are a considerable amount of the total waste, so that the costs related to their final disposal may be a high percentage of the construction costs and recycling can be an opportunity.

A way to recycle C&DWs consists in the partial substitution of natural aggregates (NAs) in concrete mixtures, after crushing and generation of recycled concrete aggregates (RCAs) from C&DWs. In this spirit, the European Union [2] has recently adopted a policy meant to promote the use of recycled aggregates for concrete production up to 70% (excluding soils and rocks without hazardous substances) for 2020, even for structural purposes. On the other hand, in recent years, concrete with recycled aggregates has been proven to be commercially and technically valid for both non-structural and structural applications [3–6].

In the international context there are a few guidelines for approaching RCAs introduction in concrete mixes [7–11]; basically, they all include in this class different sources of C&DW: crushed concrete, crushed masonry and mixed demolition debris. In some cases a definition of a maximum percentage of replacement of NAs with RCAs is recommended. The Italian standard [12] admits the use of RCAs for structural concrete in a maximum amount, related to the design strength of the final concrete and based on the origin of the recycled material.

It is commonly agreed that for high percentages of RCAs in the mixture, the effect of this replacement on the physical or mechanical properties of the mixture itself may vary, due to the presence in concrete of RCAs with adhered mortar around the aggregates, in contrast with conventional concrete [13]. This makes such a concrete a two-phase material made of the original aggregates and a variable amount of attached mortar from pre-existing cement paste.

Particularly, there is evidence that the old mortar is characterized

---

by the presence of micro-fractures due both to the original mix and to the undertaken demolition process, therefore, a higher porosity is proper of this phase [14,15].

In general, when comparing a conventional concrete with a concrete incorporating RCAs, being the slump and size distribution of the aggregates equal, there is no consensual trend in the scientific literature in terms of compressive strength: in some cases [16,17], the strength is shown to decrease at increasing fraction of coarse RCAs, while in others there is no statistically-significant change [18]. On the contrary, the modulus of elasticity significantly decreases linearly with the increasing fraction of coarse RCAs, which can be explained by the greater deformability of the adhered mortar [19].

A study made by Soares et al. [20] on the durability and mechanical performance of RCAs from precast concrete elements proves that coarse recycled aggregates from precast elements can be used to produce new concrete (up to 100% replacement ratio) without losses in terms of compressive and tensile strength and abrasion resistance, if combined with a superplasticizer.

The physical and mechanical characteristics of different kind of C&DW obtained from selective and traditional demolition techniques are investigated in Ref. [21] showing that the use of superplasticizer, combined with selective demolition, can improve significantly the mechanical properties of mortars produced with C&DW aggregate.

Given that from experimental evidences the mechanical response of concrete made with RCAs is quite complex, it can be conveniently investigated numerically via a meso-scale approach, and so at the scale of the RCAs composing the mix [22–24].

Meso-scale models can be developed by following the continuum theory or not (i.e. discrete models). Continuum models [25–27] imply that concrete is explicitly modelled via the Finite Element Method (FEM), in a way that specific material properties are directly assigned to each phase. This approach has the advantage of dealing with continuous fields of the state variables but may be computationally heavy.

Discrete models [28–37] in general can realistically predict crack patterns under various loading conditions, and they have been recently improved to describe the tensile cracking and the non-linear 3D response in compression, including the post-peak softening and strain localization [38].

In the present study the meso-scale analyses are conducted in agreement with the continuum theory; in particular, among the available linear and non linear material models [39–42], it has been chosen to implement a specific elasto-plastic-damaged model as a dedicated subroutine in Abaqus® environment [43] to perform mechanical analyses of concrete made with RCAs in uniaxial compression.

2. Geometrical reconstruction of RCAs

To realistically model a concrete sample [44,45], made with NAs and RCAs at the meso-scale level, a laser scanner has been used to get a digital 3D representation of the external geometry of a few single samples of aggregates from recycled concrete. This technology is ideal for the measurement and inspection of contoured surfaces and complex geometries which require a massive amount of data for their accurate description. Typically, with this method, point clouds are generated out of the capture of free-form shapes by a laser probe, as it is driven around the object, while two sensor cameras continuously record the changing distance and shape of the laser line in 3D. The process is very fast and precise.

One of the scanned prototypes of RCAs is reported in Fig. 1; it is evident that a RCA looks quite irregular in shape and it is characterized by two phases: a natural aggregate fully or partially embedded in the attached old mortar.

The few scanned prototypes, for which a geometrical reconstruction was accomplished, have been then properly scaled and used in combination with or without the attached mortar to simulate a realistic set

Fig. 1. Typical recycled concrete aggregate, a two-phase material made of a natural aggregate embedded in old mortar.

of NAs and RCAs in the mix design for the purposes of the FEM analysis discussed in Section 4.

In this Section the procedure to fully reconstruct the geometry of the RCA object, starting from the laser scanning, is explained in detail. Clearly, the 3D scanning technique allows to identify with high precision the external surface of the object but not the interface between the two phases, which remains unknown.

Particularly, Fig. 2 outlines the whole procedure: a point cloud is collected and, via the Geomagic® software package, it is merged into surfaces by producing a high-precision tessellation of the external area (Fig. 2 b). Then, an external geometry is generated (see e.g. Fig. 2 c), with 545 surfaces), which is simplified into one made by 114 surfaces only (Fig. 2 d) with the aid of a CAD tool; such remarkable simplification is necessary to build up a FEM model with reduced computational times but with a reasonably approximated surface. In fact it allows a general smoothing of those zones characterized by local distortions, which might require a serious mesh refinement of the solid model, so leading to a relevant increase in the number of elements.

At this point, the reconstruction of the inner boundary surface, between the embedded NA and the mortar, which is unknown since the laser scanning detects only the external surface, is mandatory for the generation of the corresponding solid model. This step has been accomplished through the definition of a certain number of cutting planes (Fig. 3 a); in correspondence of the intersection points between the two phases on the cut sections the boundary curves on each cutting plane have been traced considering the restriction for these curves to be of class C_1 (i.e. differentiable, with continuous first derivative) (Fig. 3 b). The boundary curves, so defined on many cutting planes, are auxiliary edges of an acceptable volume describing the embedded natural aggregates in this reconstruction procedure (Fig. 3 c).

The resulting solid model (Fig. 4), now distinguished into closed volumes of NAs and mortar, has been subsequently discretized in space.

In the numerical models no mesh compatibility is required at this step between mortar and embedded aggregate composing the RCA, as well as between the surface of the RCA and the surrounding cement matrix. In fact realistic adhesion properties have been assigned to the two interfaces via a contact algorithm, as described in Section 4.2.

3. Random distribution algorithm

The statistical characterization of the microstructure and its effect on the physical properties of the material have been treated fully in Torquato [46].

A so-called Random Sequential Adsorption algorithm is proposed in Ref. [47] to model materials with randomly distributed inclusions. The method developed there is hierarchical, in the sense that the well-known method of separating axis is designated as the main engine for checking whether or not the inclusions intersect each other in 3D space. However, due to the big computational cost of this method, to increase
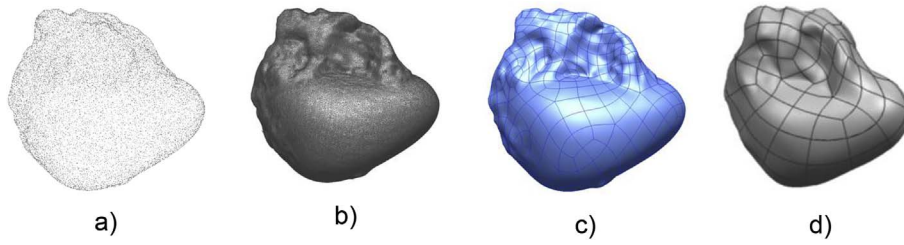
Fig. 2. 3D scan data output (point cloud) a); graphic elaboration into surfaces (tessellation) b); external surface c); simplified geometry d).

computational efficiency a series of less costly methods precedes this one, i.e.: the method of radial distances and the method of separating planes.

In this work, the method of radial distances is implemented to reproduce a realistic volume fraction of a concrete sample made with RCAs with satisfactory computational speed and in line with the stochastic techniques mentioned above.

The method involves the estimation of the radial distance between the aggregates being currently added and all the previously generated inclusions. The larger set is reduced to a small subset by considering the aggregates in the proximity being added and excluding all those in the far field.

The method of radial distance implies that an inclusion of any shape (of NAs or RCAs) can be inscribed into a "virtual" sphere (see Fig. 5 a) of diameter equal to the corresponding nominal diameter of the sieve passing in the assigned grading curve of the mix design. The total number of spheres, necessary to fill the sample, corresponds to the number of aggregates which can be evaluated in relation to the percentage of volume, i.e. the design aggregate volume fraction.

Two inclusions that are at a radial distance greater or equal to the sum of the radii of the two spheres (plus an offset distance defined for convenience in order to avoid contact) from the centre of the inclusion being added, do not intersect.

Therefore the algorithm requires the computation of the minimum distance between two close spheres d_{min}:

$$d_{min} = R_1 + R_2 + O \tag{1}$$

where R_i is the radius of the *i-th* sphere and O is the possible set between two spheres.

The distance between two spheres is, in general, computed as the square root of the square distances of the Cartesian coordinates of the centres:

$$d = \sqrt{\Sigma_{j=1}^3 (x_{2,j} - x_{1,j})^2} \tag{2}$$

where $x_{i,j}$ is the *j-th* coordinate of the sphere *i*.

Through this procedure, inclusions of higher diameters are added first. In fact, the packing density depends on the sequence of aggregate addition. For example, if larger aggregates are added first, the final packing density tends to be higher than if smaller aggregates are placed first.

Once the volume fraction is attained for such diameters, inclusions with decreasing diameters are gradually added.
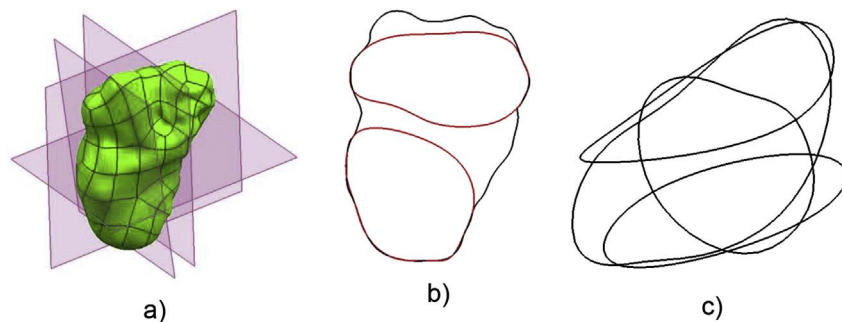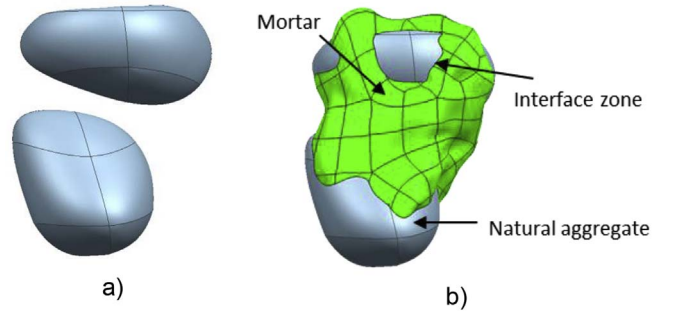

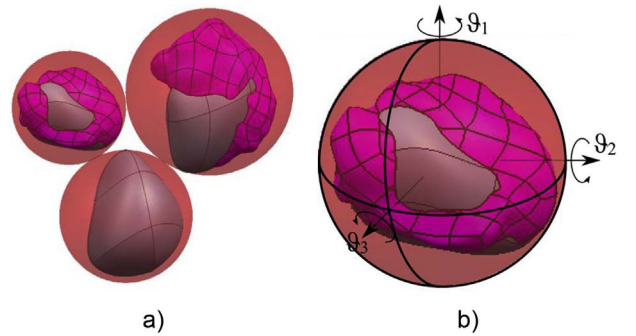**Fig. 4.** Reconstructed aggregates a); new geometry with mortar and aggregates b).

Fig. 5. Aggregates surrounded by virtual spheres a); 3D rotation angle b).

The first aggregate is generated via a random allocation of the coordinates of the centre of the circumscribed sphere, i.e. via a random function, and so on for the next *k*th sphere:

$$C(k)(x, y, z) = rand(k) \tag{3}$$

Considering the irregular shape of the aggregates, a random solid rotation angle has been defined also, with the use of a similar random function of components:

$$\vartheta(i) = rand(i)(i = 1,2,3) \tag{4}$$

where *i* stands for the direction of the local axis of the *k*th sphere in space (Fig. 5 b).

Fig. 3. Characteristics cut planes a); perimeter of NAs in a cut plane b); NAs edges c).
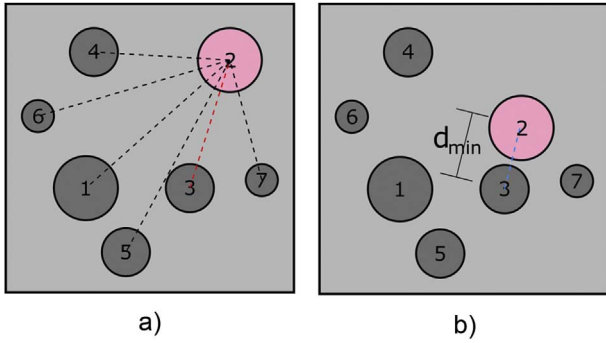
Fig. 6. Packing algorithm for aggregate #2: effective minimum distance $d_{eff,min}$ with all the other aggregates a); reduction of $d_{eff,min}$ to d_{min} b).

Therefore, each aggregate is made to vary randomly in function of two variables: its centre and its orientation.

From the second inclusion onwards, the inclusion being added is checked for intersection with all the previously generated, nearby, via the radial distance method. The new inclusion is successfully placed if there is no intersection, otherwise it is discarded and a new one is generated.

A specific packing algorithm allows for the optimum use of space. In fact, a forced packing scheme is implemented based on the computation of the minimum distance between the current inclusion and all the previous ones, which leads to reject all the configurations that prevent the highest possible packing. This check is made every n aggregates included in the sample, where n is an input parameter of the algorithm.

Finally, the geometry at the meso-level is described by the co-ordinates of the centre of the circumscribed sphere and the angle of rotation of the inclusions.

The packing algorithm is schematically illustrated in Fig. 6: once the minimum distance $d_{eff,min}$ between the current aggregate, with respect to all the other aggregates in the sample, is detected, this distance is reduced to d_{min}, if this rigid motion does not bring compenetration into existing bodies.

In order to implement the algorithm, the RCAs and NAs volume fraction, the grading curve and the geometry of the inclusions are all user-defined parameters.

The random distribution algorithm is outlined by the flowchart in Fig. 7 and it is described below:

(i) For a randomly generated centre $C(x,y,z)$ of the circumscribed sphere and angle of rotation $\Theta(\vartheta_1, \vartheta_2, \vartheta_3)$ of the inscribed aggregate in 3D space, a first inclusion is generated, starting from the bigger diameter, to allow the maximum compaction.

(ii) From the generation of the second inclusion up to the insertion of the last particle, belonging to the lowest diameter range of the assigned grading curve, the random scheme is applied for centres and angles of rotation of the next inclusions, checking at each time whether any intersection occurs between the spheres, and so between the aggregates.

(iii) If the newly generated inclusion satisfies the minimum distance algorithm, i.e. it does not intersect with any other previously generated, then the inclusion is generated in space. The aggregate volume fraction is updated and the algorithm moves on to generate the next inclusion. If, after a predefined number of trials, the newly generated inclusion has not found its place so that it does not overlap with existing inclusions, then it is discarded and the algorithm calls back the random generation of centres and angles of rotation of a next inclusion in the same manner.

(iv) If any part of the inclusion lies outside the sample edges, the inclusion is discarded as well.

(v) Steps (i) to (iv) are repeated for all the fractions of all the nominal diameters of the particles until the required aggregate volume fraction V_f is achieved.
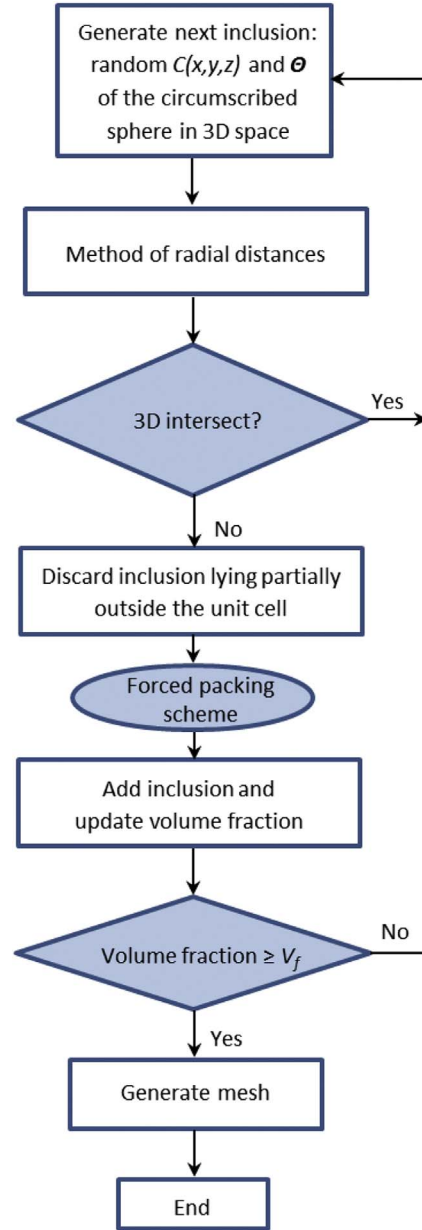

Fig. 7. Flowchart of the algorithm for a random inclusion distribution within a concrete sample made of NAs and RCAs of assigned grading curve and volume fraction.

(vi) Once the geometry of the internal distribution has been re-constructed, mesh discretization is possible for the next FEM analyses.

This algorithm has been developed in Visual Basic language and it has been equipped with a user interface for the assignment of the necessary input data.

An example of the output of the presented algorithm, for a concrete sample made of RCAs and NAs, randomly placed and oriented, and characterized by a trial grading curve and a given volume fraction, is reported in Fig. 8. This simulation corresponds to a volume fraction of aggregates of 78%, of which: 70% is made by NAs and 30% by RCAs.

The key feature of the proposed algorithm is the capability to quickly generate random, high-packing fractions in volume of aggregates, with a wide range of diameters, and with an assigned grading curve.

As already mentioned, the packing density depends on the addition sequence of new inclusions, which is the reason why bigger aggregates
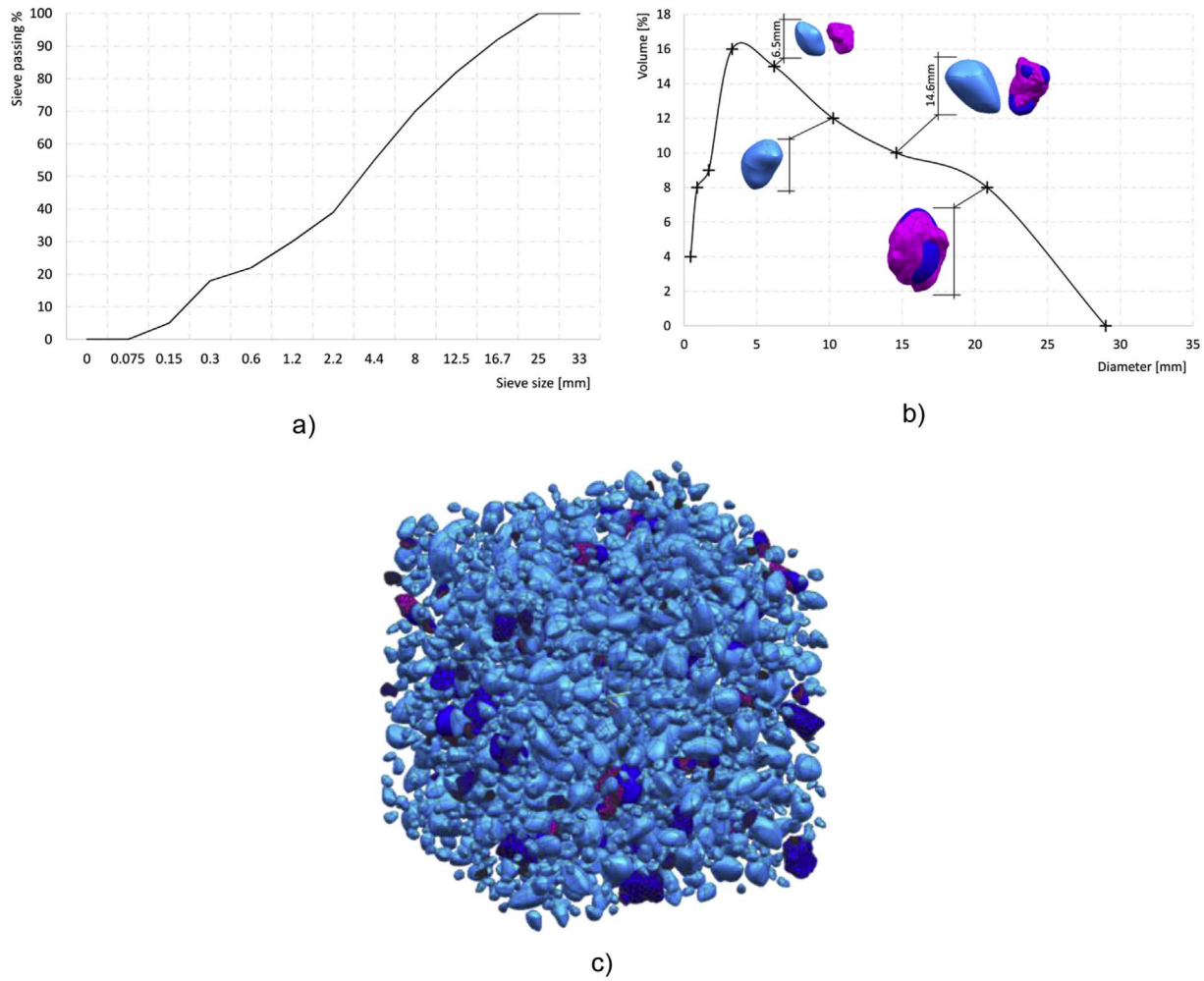
a)

b)

c)

Fig. 8. Example of aggregate random distribution from assigned grading curve to a realistic 3D model (sample $25 \times 25 \times 25$ mm^3; aggregate nominal diameter ranging: 0.9–28 mm; aggregate volume fraction: 78%, of which: 70% NAs and 30% RCAs).

are inserted first. Therefore, the maximum number of trials of new inclusions satisfying the minimum radial distance algorithm, as well as the maximum number of iterations necessary to reach the optimum packing configuration, must be carefully chosen so to achieve a final volume fraction closest to the theoretical one, in acceptable computational times.

4. Numerical analyses

4.1. Grading curve and mix design

The grading curve reported in Fig. 9 is at the basis of the concrete mix design adopted in the numerical analyses; this curve is expected to well reproduce the optimum compaction of the aggregates in agreement with the Bolomey law, computed for a maximum size of aggregates in the mixture of 22.4 mm and a coefficient, depending on the shape of the aggregates and on the consistency class, equal to 12.

The mixture is composed by 350 kg/m^3 of cement CEM I 52.5R with a w/c equal to 0.45. The global volume of aggregates is distributed as follows: 9.2% of RCAs, 39.8% of NAs (gravel) and 51% of NAs (sand).

It is reasonable to model at the meso-scale only the coarse fraction (RCAs and NAs gravel), neglecting all inclusions of diameter less than 5 mm, which can be considered as part of the concrete matrix surrounding the aggregates as a homogeneous material, since they are generally conceived as fine fraction.

The volumes corresponding to cement (V_{cement}) and water (V_{water}) in
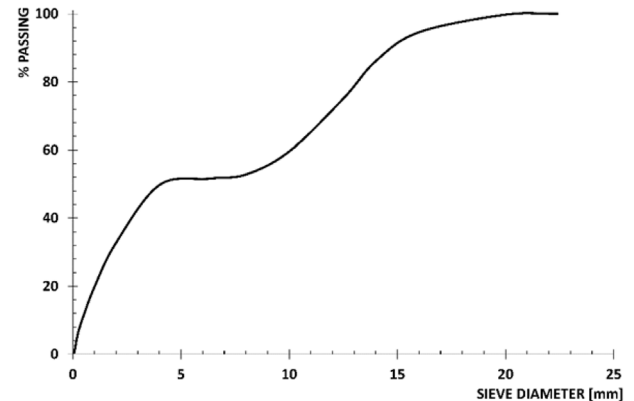

Fig. 9. Grading curve adopted for the concrete mix design of the FEM analysis.

the total volume follow from the assumption of the cement and the water densities: $\rho_c = 3000$ kg/m^3 and $\rho_w = 1000$ kg/m^3, respectively.

Therefore $V_{cement} = 350/300 \approx 0.12$ and $V_{water} = 157/1000 \approx 0.16$.

The volume of the total aggregates for each m^3 of concrete is evaluated, then as: $V_{aggr} = 1 - V_{cement} - V_{water} \sim 0.73$.

Therefore, the volume of the coarse fraction is: $V_{aggr, \, coarse} = (9.8\% + 39.2\%)V_{aggr} \sim 0.36$ or 36% per m^3 of concrete, of which almost 20% consists in RCAs and 80% in NAs.
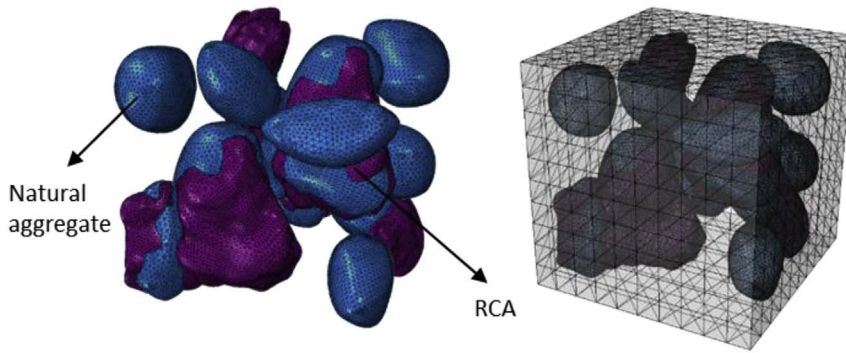
Fig. 10. Example of a FEM model of a concrete sample made of RCAs and NAs, obtained from the solid model of laser scanned RCAs.

4.2. ITZ definition with contact algorithm

After some RCAs have been laser-scanned, so that to reconstruct their overall geometry and produce the corresponding solid models (as illustrated in Section 2), the last have been introduced in a realistic concrete sample, which satisfies a given grading curve and volume fraction, by combining NAs with RCAs of different sizes, randomly in the sample domain.

An example of the combination of RCAs and NAs into a FEM model, with the surrounding cement paste filling the sample, is reported in Fig. 10, where the discretization in space of the different volumes (matrix and inclusions) can be appreciated.

When modelling concrete at the meso-scale with the continuum approach (FEM), the Interfacial Transition Zone (ITZ) between the aggregates and the cement paste is generally not neglected [48,49], since this region has properties which are known to influence the stress-strain relationship and the failure patterns of concrete [50]. The ITZ, in the case of concrete made with RCAs, can also affect as a thin layer the interface between the attached mortar and the embedded NAs, and not only the interface between the aggregate and the cement matrix. As commonly agreed, the ITZ is characterized by a higher porosity and a higher permeability with respect to the cement paste [51,52], locally reducing the mechanical characteristics of the matrix.

In this paper, however, it has been chosen not to explicitly model ITZ; apart for saving computational times, the main reason is twofold: as reported elsewhere in literature, the influence of ITZ can be more appreciated when considering hygro-thermal issues, having in fact in mind its more porous structure if related to cement paste. However, its contribution is smaller if aggregates are porous (as in case of recycled aggregates), having a reduced stagnation of water around them. Additionally, no hygro-thermal analyses are performed in the paper.

Then, even considering just the mechanical behaviour and the lower strength of ITZ if compared to cement paste, the spreading of damage within the sample is not affected by ITZ but by aggregates and aggregates distribution. In case ITZ can affect the *instant* of triggering for damage, but such an aspect cannot be caught by quasi-static analyses.

4.3. Local confinement

It is well known, e.g. in confined concrete columns during compression loads [53,54], that the stress-strain or the force-displacements relation changes at varying degree of the lateral confinement. At different confinement levels, or different hydrostatic pressure, a softening or a hardening behaviour may occur (see Fig. 11); in fact, by increasing the hydrostatic pressure, the softening branch progressively changes its slope up to a hardening configuration.

In a meso-scale approach the presence of aggregates, with different stiffness with respect to the surrounding matrix, implies a local confinement effect (LCE) of the cement paste around the aggregates themselves. The LCE may vary considerably within the concrete sample and it is related to the relative distance between the aggregates, their
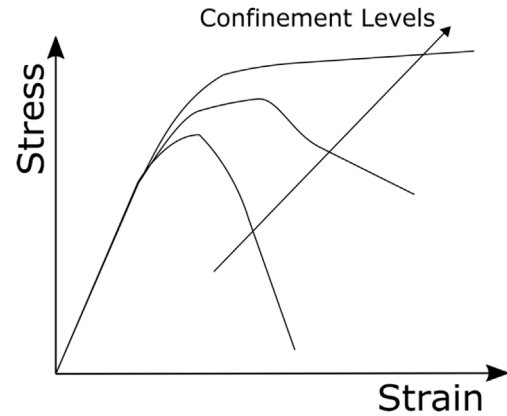

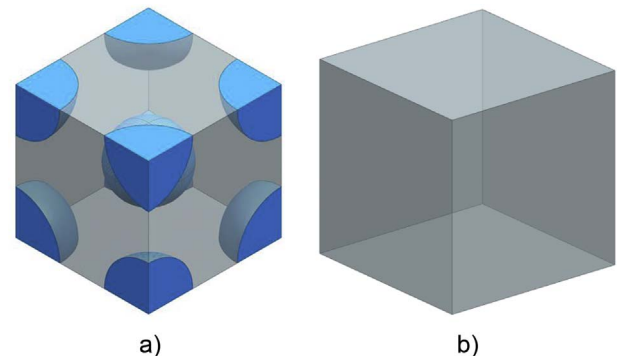**Fig. 11.** Stress vs. strain curves at different levels of confinement.

Fig. 12. Local confinement model in meso-scale a) and macro-scale b).

Table 1
Mechanical characteristics for the macro- and meso-scale elastic models.

Model	E_m [MPa]	μ_m	E_a [MPa]	μ_a
Macro	30000	0.15	–	–
Meso	30000	0.15	60000	0.15

stiffness and their dimensions.

For example, let us consider two simplified cubes (see Fig. 12), of dimensions $60 \times 60 \times 60 \, mm^3$, composed by 9 spherical aggregates having a diameter of 40 mm, symmetrically disposed. Table 1 reports the elastic constitutive properties for the macro- and the meso-scale models. The sample is subjected to a compressive load and statically determinate boundary conditions. When plotting the hydrostatic pressure for the two models (see Fig. 13), the confinement is found to increase of about 72% in the sample with aggregates if compared to the homogeneous model.
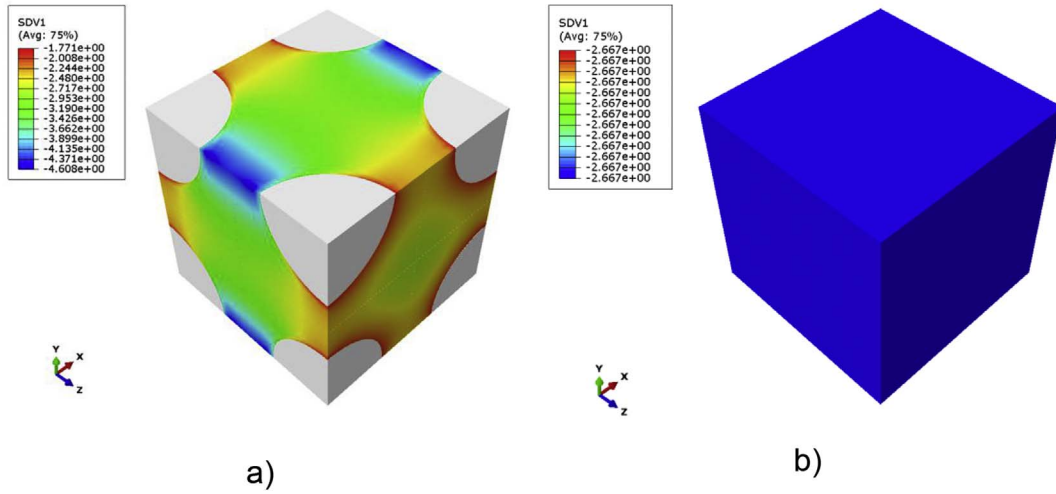
Fig. 13. Hydrostatic pressure: meso-scale a) and macro-scale b) models.

In this example the distance between the aggregates is of about 20 mm (this value does not meet the maximum compaction condition, generally assumed in a concrete mixing), sufficient to observe that a meso-scale approach is affected by a LCE, which is not caught by a macro-scale formulation. This LCE is responsible for a variation in the local stiffness of the cement matrix in presence of a compression load.

Obviously, the confinement condition can additionally increase if the distance between aggregates is reduced and/or statically indeterminate boundary conditions occur.

4.4. Constitutive law

The performed numerical analysis simulates a uniaxial compression test and it is aimed to assess the mechanical behaviour of a concrete sample made partially of NAs and RCAs.

A clear distinction in the volume fractions has been achieved through the reconstruction procedure illustrated in Section 3, and then the volumes have been discretized in space, as discussed in Section 4.

At this point, a specific constitutive behaviour has been assigned to each phase: NAs have been considered to behave elastically while an elastic-plastic law with damage has been assigned to the attached mortar and the cement matrix, which are likely to crack first, under compressive loads.

Particularly, a damage-plasticity model consists in the combination of non-associated plasticity [55] and a scalar (isotropic) damage model that allows for describing the irreversible damage process occurring during load evolution.

The constitutive model assumes the following stress-strain relationship:

$$\boldsymbol{\sigma} = (1 - \omega)\boldsymbol{D_e} : (\boldsymbol{\varepsilon} - \boldsymbol{\varepsilon^{pl}}) \tag{5}$$

where $\boldsymbol{\sigma}$ is the Cauchy stress tensor; ω is the scalar damage parameter [56–58]; $\boldsymbol{D_e}$ is the elastic stiffness material tensor; $\boldsymbol{\varepsilon^{pl}}$ is the plastic strain, and $\boldsymbol{\varepsilon}$ is the total strain tensor, so that $\boldsymbol{\varepsilon} - \boldsymbol{\varepsilon^{pl}}$ is the elastic strain $\boldsymbol{\varepsilon^{el}}$.

The plasticity model for concrete is based on Menétrey-Willam plastic surface [55,59], where the yield surface is described in function of the second and the third deviatoric invariants of the stress tensor, J_2 and J_3, based on the Haigh-Westengard (HW) coordinates (ξ, ρ, θ):

$$\xi = \frac{I_1}{\sqrt{3}f_c}; \rho = \sqrt{2J_2}; \cos(3\theta) = \frac{3\sqrt{3}}{2}\frac{J_3}{J_2^{3/2}} \tag{6}$$

where I_1 is the first invariant of the stress tensor $\boldsymbol{\sigma}$ ($I_1 = \sigma_{ii}$). Let us name the deviatoric stress tensor $\boldsymbol{S}$, of components s_{ij}, then the second and the third invariants are defined as:

$$J_2 = \frac{1}{2}s_{ij}s_{ij}; J_3 = \frac{1}{3}s_{ij}s_{jk}s_{ki} \tag{7}$$

The yield surface takes the following expression:

$$f_p = \frac{3}{2}\rho^2 + q \cdot m\left(\frac{\rho r(\theta)}{\sqrt{6}} + \frac{\xi}{\sqrt{3}}\right) - q \le 0 \tag{8}$$

where q is the plastic softening law [60], function of the equivalent strain $q = q(\varepsilon^{eq})$. In this work ε^{eq} has been taken equal to the volumetric plastic strain $\varepsilon^{eq} = I_1(\varepsilon^{pl}) = \varepsilon^{pl}_{(i,i)}$.

The r parameter is an elliptic function depending on the lode angle θ and on the material eccentricity e:

$$r(\theta, e) = \frac{4(1 - e^2)\cos^2(\theta) + (2e - 1)^2}{2(1 - e)^2\cos(\theta) + (2e - 1)\sqrt{4(1 - e^2)\cos^2(\theta) + 5e^2 - 4e}} \tag{9}$$

The eccentricity e gives the roundness of the yield surface, while the parameter m is defined as:

$$m = 3\frac{f_c^2 - f_t^2}{f_c f_t}\left(\frac{e}{e + 1}\right) \tag{10}$$

In Fig. 14 the yield surface in the deviatoric plane for different hydrostatic pressures is reported.

A non-associated flow rule is considered and the plastic potential is defined in agreement with [59]:

$$g_p = -A\left(\frac{\rho}{\sqrt{q}}\right)^2 - B\frac{\rho}{\sqrt{q}} + \frac{\xi}{\sqrt{q}} = 0 \tag{11}$$
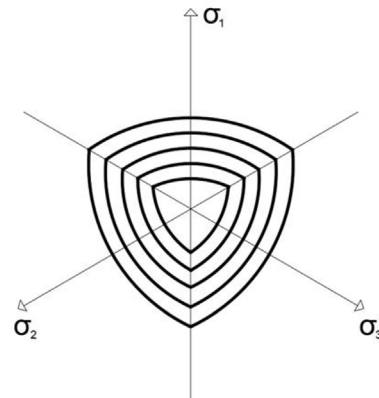

Fig. 14. Yield surface at different hydrostatic pressures.

where A and B are experimentally derived coefficients.

The plastic law has been coupled with damage [61–64], where the damage variable ω is a stiffness degradation parameter which gives the reduction of the initial (undamaged) modulus of the material E_0, both in tension and in compression: $E = (1-\omega)E_0$, in uniaxial state.

The implemented isotropic damage law is in agreement with Mazars' theory, i.e. ω is a combined expression of damage in tension ω_t and in compression ω_c:

$$\omega = \alpha_t \omega_t + \alpha_c \omega_c \tag{12}$$

where α_t and α_c are weight functions; they take values between 0 and 1 [56].

The two damage variables are assumed functions of the plastic strains and their evolution laws depend on the material parameters A_t, A_c, B_t, B_c, that can be estimated through uniaxial compression ($i = c$) or tension ($i = t$) tests:

$$\omega_i(\bar{\varepsilon}) = 1 - \frac{(1 - A_i)K_0}{\bar{\varepsilon}} - \frac{A_i}{exp\,[B_i(\bar{\varepsilon}) - K_0]} \quad (i = t, c) \tag{13}$$

where $\bar{\varepsilon}$ is the average equivalent strain as defined in Mazars and Pijaudier-Cabot [57].

The plastic-damage combination theory based on the effective stress has been followed [65]. By taking the loading function vector $\mathbf{f}$ and the internal variable vector $\boldsymbol{\lambda}$ as:

$$\dot{\mathbf{f}} = \begin{bmatrix} \dot{f}_p \\ \dot{f}_d \end{bmatrix} \quad \dot{\boldsymbol{\lambda}} = \begin{bmatrix} \dot{\lambda}_p \\ \dot{\lambda}_d \end{bmatrix} \tag{14}$$

the Kuhn-Tucker condition is satisfied:

$$\dot{\mathbf{f}} \le 0, \quad \dot{\boldsymbol{\lambda}} \ge 0, \quad \dot{\boldsymbol{\lambda}}^T \dot{\mathbf{f}} = 0 \tag{15}$$

with $\dot{\mathbf{f}}$ defined as $\dot{\mathbf{f}} = \mathbf{b} - \mathbf{A}\dot{\boldsymbol{\lambda}}$, where:

$$A = \begin{bmatrix} \frac{\partial f_p}{\partial \sigma} : \mathbf{D}_e : \frac{\partial g_p}{\partial \sigma} & 0 \\ -\frac{\partial f_d}{\partial \varepsilon_p} : \frac{\partial g_p}{\partial \sigma} & \frac{\partial f_d}{\partial k_d} \end{bmatrix}; \; b = \begin{bmatrix} \frac{\partial f_p}{\partial \sigma} : \mathbf{D}_e : \dot{\varepsilon} \\ \frac{\partial f_d}{\partial \varepsilon} : \dot{\varepsilon} \end{bmatrix} \tag{16}$$

4.5. Model calibration

To calibrate the composite sample at the meso-scale level, the calibration of its single constituents is mandatory. Therefore, a homogeneous sample of cement matrix (CM) is first considered; specific compression tests on CM samples have been carried out to evaluate the stress-strain curve and consequently calibrate the mechanical behaviour of the matrix. A C50 cement-type sample has been subjected to a compressive load. The comparison between experimental evidences [66] and numerical curves in terms of stress vs. strain is reported in Fig. 15.
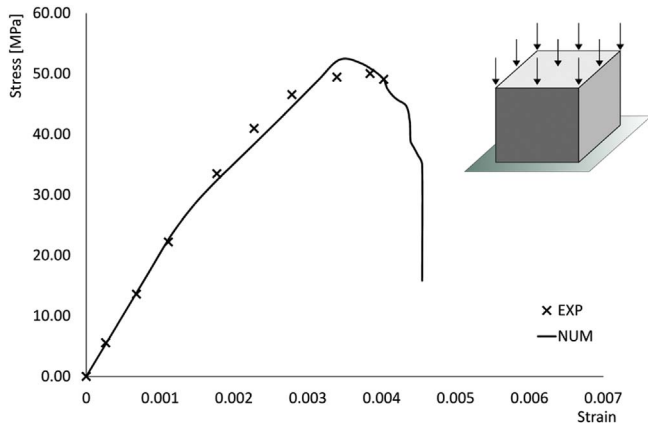
Fig. 15. Numerical calibration of CM in terms of stress vs. strain curve.

Table 2
Cement matrix parameters after calibration.

Young's modulus [MPa]	20000
Poisson's coefficient	0.15
f_c [MPa]	−50.00
f_t [MPa]	5.00
e	0.52
ε_v^{pl}	0.0017
K_0	0.20
A	6.427
B	−12.827

Table 3
Damage parameters after calibration.

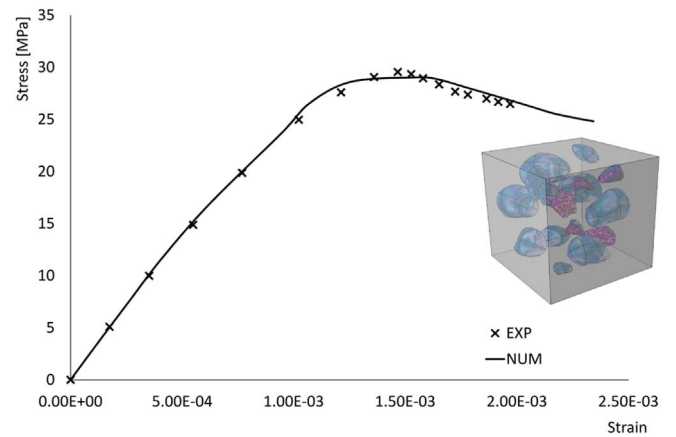|			
$K_{0,c}$	0.00124	$K_{0,t}$	0.0
A_c	1.0	A_t	1.0
B_c	300.0	B_t	1000.0

Fig. 16. Meso-scale calibration in terms of stress vs. strain curve.
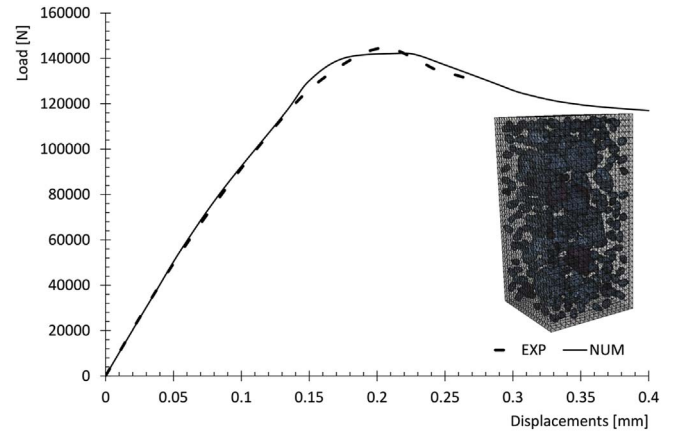
Fig. 17. Load vs. displacement response.

The elasto-plastic parameters obtained through this calibration are listed in Table 2.

The damage parameters are assumed in agreement with the ranges suggested by Mazars, relative to ordinary concrete (see Table 3):

Once the cement matrix has been characterized, for the remaining components the following reasonable assumptions have been made: the mechanical characteristics of the mortar around the RCAs have been assigned equal to those of a damaged concrete with a low compression strength $f_{c,RA} = 3$ MPa and an initial elastic modulus equal to $E_{RA} = 20$ GPa, while a compression strength equal to $f_{c,NA} = 45$ MPa and an initial Young's modulus equal to $E_{NA} = 50$ GPa have been

assigned to the NAs.

The calibration of the composite has been conducted on a cubic sample of dimensions $35 \times 35 \times 35 \, mm^3$ and a grading curve corresponding to the one of the tested sample. Inerts having dimensions greater than 4 mm have been included in the model (Fig. 16).

4.6. Numerical results

After the calibration phase, the overall behaviour of the composite has been validated for a prismatic concrete sample $70 \times 70 \times 140 \, mm^3$; the grading curve for the mix design corresponds to the one reported in Fig. 9.

The sample consists in 373 aggregates in total, among which are NAs and RCAs, of different sizes (comprised between 4 mm and 16 mm); their position inside the sample is determined via the random distribution algorithm previously described. The aggregates which have not been explicitly modelled, due to their negligible dimensions, have been taken into account by averaging their properties over those of the cement matrix.

The constitutive characteristics are derived from the calibration phase illustrated in the previous Section, for each constituent.

Bottom and top surfaces have been fixed in order to avoid in-plane translations and a monotonic axial compressive load has been assigned to the sample until failure.

The obtained load-displacement behaviour of the sample is reported in Fig. 17.

Fig. 18 illustrates damage evolution in the sample, the red zone representing the region with a damage variable greater than 80%; an irregular distribution of damage is envisaged, which must depend on the aggregates distribution. Notably, damage is shown to trigger near the core aggregates, in correspondence of over-stressed zones caused by different materials stiffness. The real behaviour of the sample, according to which a global delay in the development of softening occurs, is hence correctly caught by LCE, depending on a representation at a meso-scale level, as well as by the choice of a specific plastic potential (Eq. (11)).
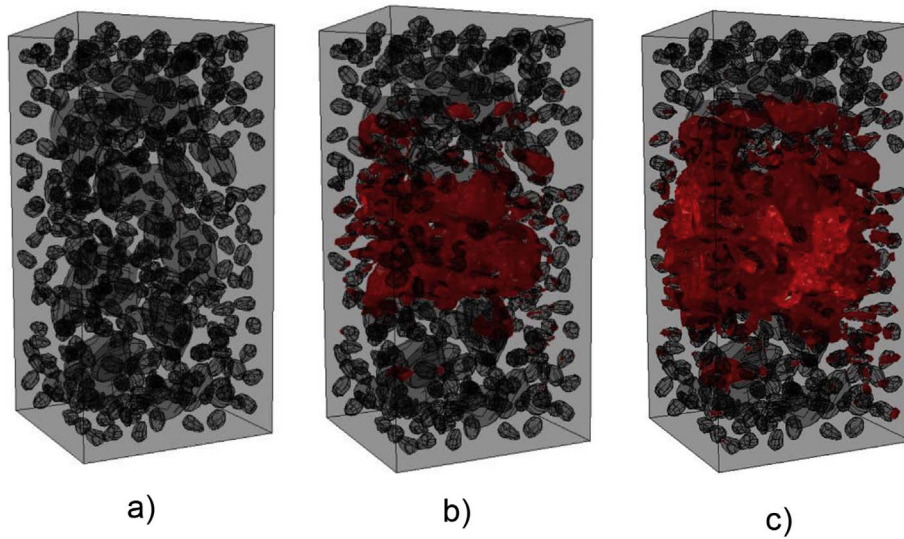

Fig. 18. Damage evolution in the sample at different times: at 30% a); 80% b); 100% c) of the total applied load.
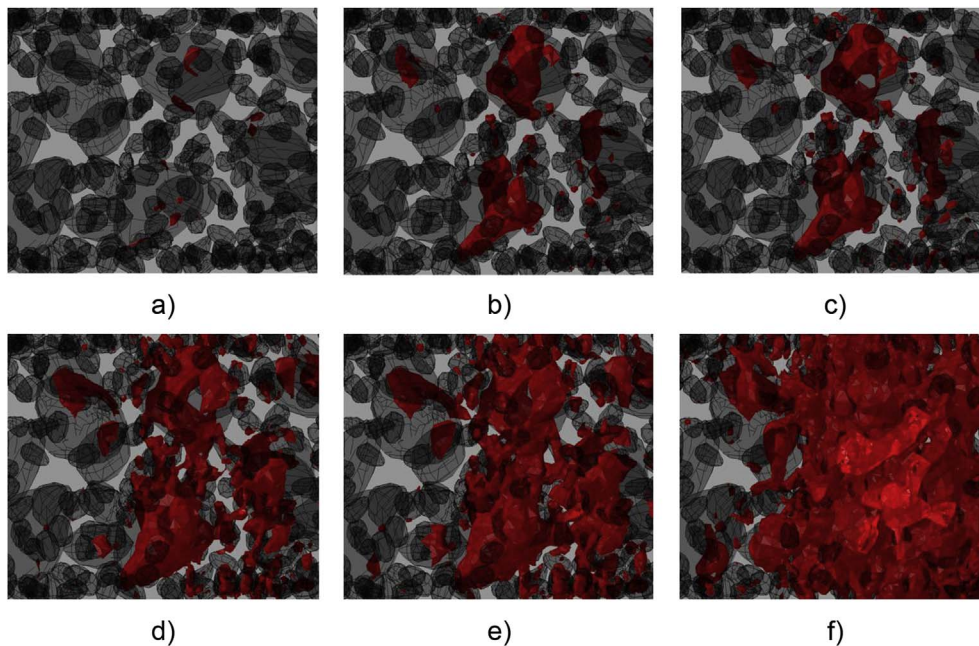
a)   b)   c)

Fig. 19. Damage evolution in a local zone of the sample at different times: at 30% a); 50% b); 60% c); 80% d); 90% e); 100% f) of the total applied load.
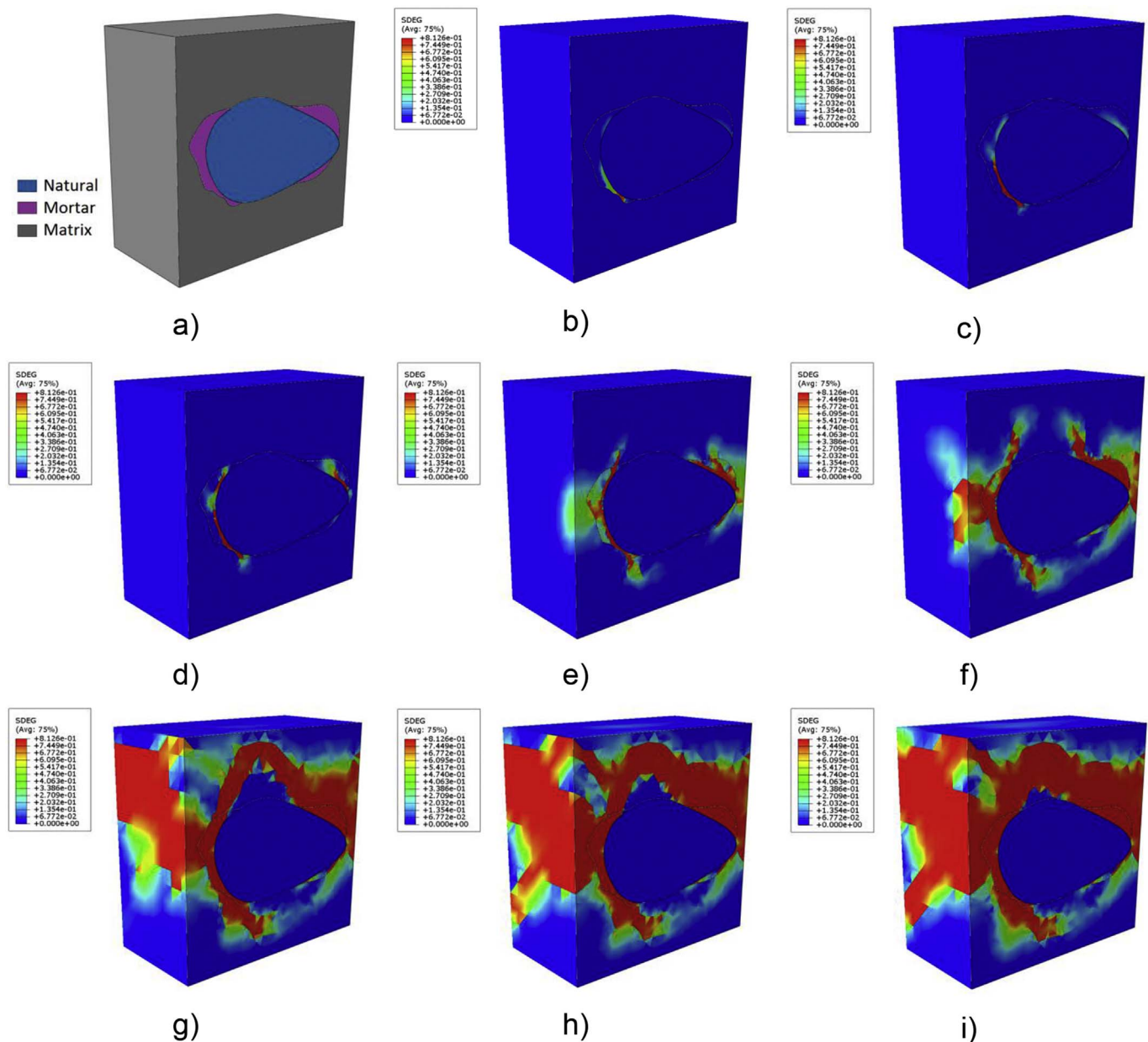
a)   b)   c)

d)   e)   f)

Fig. 20. Geometric configuration of a single RCA a); damage evolution during the compression test analysis in a local zone around the RCA b-i).

Particularly, the development of damage from the core aggregates to the surrounding cement matrix is evident (see Fig. 19 a and b). Damage is shown to evolve into "random" damaged zones (RDZs), which depend on many factors such as the shape of the aggregates and the differential stiffness between RCAs and NAs.

At a low load, the RDZ is small and the global concrete stiffness is not much influenced; therefore, it is expected that the behaviour does not differ too much from the homogeneous mesoscopic one. Under a further increase in load, damage propagates within the cement matrix (see Fig. 19 c) until the RDZ converges into a "macro" damaged zone (MDZ) (see Fig. 19 d–f); consequently, the global stiffness of the sample is reduced and softening occurs.

The RDZ evolution can be better caught if a local portion around a single recycled aggregate is considered (Fig. 20 a). Damage starts at the interface between natural aggregate and mortar (Fig. 20 b), i.e. the zone characterized by the maximum variation in stiffness between the components of the RCA. Under increasing load, damage first migrates towards the mortar, which represents the weaker fraction of the RCA

(Fig. 20c and d), then it develops into the cement matrix (Fig. 20e–i), showing the typical crushing failure of a sample, with cracks first spreading around the aggregates up to detachment of aggregates themselves and complete fragmentation of the matrix. Hence, at the first stage of spreading of damage, the surrounding cement matrix is confined and a hardening-type behaviour occurs with correspondent increase in global concrete strength; subsequently, with damage propagation within the matrix, the effective sample failure occurs.

5. Conclusions

The challenging aspects of modelling recycled aggregates from demolition waste in concrete mixtures are pointed out in this paper and a formalized procedure is suggested to reconstruct such a complex composite material at the meso-scale level.

An accurate reproduction of the geometry of these aggregates has been accomplished through the aid of a 3D laser scanning technique. The obtained geometry has been reasonably simplified via a CAD

software to reduce the computational effort; starting from the external surface geometry, a method to distinguish the inner volumes of these multiphase objects has been studied, which allowed the generation of a solid model and its use for FEM analyses.

A realistic concrete mix design has been defined, partially composed by natural aggregates and partially by recycled aggregates. For this purpose, an *ad-hoc* random algorithm has been developed to place and orient the inclusions within a concrete sample, satisfying the volume ratio of the aggregates and the given grading curve. Only the coarse fraction of the aggregates has been numerically modelled, which is a reasonable choice when modelling concrete at the meso-scale level.

A specific elastic-plastic-damaged formulation has been implemented and calibrated on a sample of concrete made with RCAs, in a given amount, and subjected to uniaxial compression. The plasticity model is based on Menétrey-Willam plastic surface, where the yield surface is described in function of the second and the third deviatoric invariants of the stress tensor, while the scalar isotropic model by Mazars is considered for damage.

The proposed constitutive law together with a precise meso-scale modelling have demonstrated to correctly represent and describe local confinement effects as well as the real inelastic behaviour of concrete samples.

Acknowledgements

Appendix A. Supplementary data

Supplementary data related to this article can be found at http://dx.doi.org/10.1016/j.compositesb.2017.12.018.

References

[1] Eurostat. Waste statistics in europe. 2017http://ec.europa.eu/eurostat/.
[2] Directive. 2008/98/EC of the european parliament and of the council on waste and repealing certain directives, november 19th. 2008.
[3] Shayan A, Xu A. Performance and properties of structural concrete made with recycled concrete aggregate. ACI Mater J 2003;100(5):371–80.
[4] Fathifazl G, Razaqpur AG, Isgor OB, Abbas A, Fournier B, Foo S. Flexural performance of steel-reinforced recycled concrete beams. ACI Struct J 2009;106(6):858–67.
[5] Xiao JZ, Sun YD, Falkner H. Seismic performance of frame structures with recycled aggregate concrete. Eng Struct 2006;28(1):1–8.
[6] Xiao JZ, Wang CQ, Li J, Tawana MM. Shaking table model tests on recycled aggregate concrete frame structure. ACI Struct J 2012;109(6):777–86.
[7] BCSJ. Proposed standard for the use of recycled aggregate and recycled aggregate concrete. Japan: Committee on Disposal and Reuse of Construction Waste, Building Contractors Society of Japan; 1977.
[8] BS-8500. Concrete complementary British Standard to BS EN 206-1 Part 2: specification for constituent materials and concrete. UK: British Standards Institution; 2006.
[9] DIN-4226. Aggregates for mortar and concrete, Part 100: recycled aggregates. Germany: Deutsches Institut fur Normungswesen; 2002.
[10] EHE-08. Code on structural concrete. Spain: Centro de Publicaciones, Secretaria General Tecnica, Ministerio de Fomento; 2010.
[11] RILEM TC 121-DRG. Specifications for concrete with recycled aggregates. Mater Struct 1994;27(173):557–9.
[12] Decreto del Ministero delle infrastrutture DM 14/1/2008-Norme tecniche per le costruzioni, Italy.
[13] Colangelo F, Messina F, Di Palma L, Cioffi R. Recycling of non-metallic automotive shredder residues and coal fly-ash in cold-bonded aggregates for sustainable concrete. Compos B Eng 2017;116:46–52.
[14] Silva RV, de Brito J, Dhir RK. Properties and composition of recycled aggregates from construction and demolition waste suitable for concrete production. Construct Build Mater 2014;65:201–17.
[15] Pepe M, Toledo Filho RD, Koenders EAB, Martinelli E. Alternative processing procedures for recycled aggregates in structural concrete. Construct Build Mater 2014;69:124–32.
[16] Rao MC, Bhattacharyya SK, Barai SV. Influence of field recycled coarse aggregate on properties of concrete. Mater Struct 2011;44(1):205–20.
[17] Kou SC, Poon CS. Enhancing the durability properties of concrete prepared with coarse recycled aggregate. Construct Build Mater 2012;35:69–76.
[18] Malesev M, Radonjanin V, Marinkovic S. Recycled concrete as aggregate for structural concrete production. Sustainability 2010;2(5):1204–25.
[19] De Brito J, Robles R. Recycled aggregate concrete (RAC) methodology for estimating its long-term properties. Indian J Eng Mater Sci 2010:449–62.
[20] Soares D, de Brito J, Ferreira J, Pacheco J. Use of coarse recycled aggregates from precast concrete rejects: mechanical and durability performance. Construct Build Mater 2014;71:263–72.
[21] Colangelo F, Cioffi R. Mechanical properties and durability of mortar containing fine fraction of demolition wastes produced by selective demolition in South Italy. Compos B Eng 2017;115:43–50.
[22] Contri L, Majorana CE, Schrefler BA. A structural inhomogeneous material model for concrete at early ages - modele structurele multiphase non homogene pourbeton jeune. Colloque Internationale sur le beton jeune. International conference on concrete at early ages. Paris, Avril 6-8. 1982. p. 203–13.
[23] Contri L, Majorana CE, Schrefler BA. Numerical formulation of a multi-phase composite material model for concrete. Colloque Internationale sur le beton jeune. International conference on concrete at early ages. Paris, Avril 6-8. 1982. p. 198–9.
[24] Roelfstra PE, Sadouki H, Wittmann FH. Le beton numerique. Mater Struct 1985;18:309–17.
[25] Wittmann FH, Roelfstra PE, Kamp CL. Drying of concrete: an application of the 3L-approach. Nucl Eng Des 1988;105:185–98.
[26] Carol I, Lopez CM, Roa O. Micromechanical analysis of quasi-brittle materials using fracture-based interface elements. Int J Numer Meth Eng 2001;15:120–33.
[27] Wriggers P, Moftah SO. Mesoscale models for concrete: homogenisation and damage behaviour. Finite Elem Anal Des 2006;42:623–36.
[28] Bazant ZP, Tabbara MR, Kazemi MT, Pijaudier-Cabot J. Random particle model for fracture of aggregate or fiber composite. J Eng Mech-ASCE 1990;116(8):1686–705.
[29] Schlangen E, van Mier JGM. Simple lattice model for numerical simulation of fracture of concrete materials and structures. Mater Struct 1992;25(153):534–42.
[30] Schlangen E. Computational aspects of fracture simulations with lattice models. In: Wittmann FH, editor. Fracture mechanics of concrete. 1995. p. 913–28.
[31] Van Mier JGM, Vervuurt A, Schlangen E. Bazant ZP, Bittnar Z, Jirásek M, Mazars J, editors. Boundary and size effects in uniaxial tensile tests: a numerical and experimental study. Fracture and damage in quasi brittle structures. London: E&F Spon; 1994.
[32] Lilliu G, van Mier JGM. 3D lattice type fracture model for concrete. Eng Fract Mech 2003;70:927–41.
[33] Cusatis G, Pelessone D, Mencarelli A, Baylot JT. Lattice discrete particle model (LDPM): formulation, calibration, and validation. Proc. Int. Symposium on the interaction of the effects of munitions with structures (ISIEMS). 2007. Orlando, Florida.
[34] Le BD, Dau F, Charles JL, Iordanoff I. Modeling damages and cracks growth in composite with a 3D discrete element method. Compos B Eng 2016;91:615–30.
[35] Ismail Y, Yang D, Ye J. A DEM model for visualising damage evolution and predicting failure envelope of composite laminae under biaxial loads. Compos B Eng 2016;102:9–28.
[36] Trovalusci P, De Bellis ML, Masiani R. A multiscale description of particle composites: from lattice microstructures to micropolar continua. Compos B Eng 2017;128:164–73.
[37] Fascetti A, Feo L, Nisticò N, Penna R. Web-flange behavior of pultruded GFRP I-beams: a lattice model for the interpretation of experimental results. Compos B Eng 2016;100:257–69.
[38] Marotti de Sciarra F. A general theory for nonlocal softening plasticity of integral-type. Int J Plast 2008;24:1411–39.
[39] Marotti de Sciarra F. Variational formulations and consistent finite-element procedure for a class of nonlocal elastic continua. Int J Solid Struct 2008;45(14–15):4184–202.
[40] Marotti de Sciarra F. Finite element modelling of nonlocal beams. Phys E Low-dimens Syst Nanostruct 2014;59:144–9.
[41] Marotti de Sciarra F. Variational formulations, convergence and stability properties in nonlocal elastoplasticity. Int J Solid Struct 2008;45(7–8):2322–54.
[42] Marotti de Sciarra F, Salerno M. On thermodynamic functions in thermoelasticity without energy dissipation. Eur J Mech Solid 2014;46:84–95.
[43] ABAQUS Version 6.12-1. ABAQUS 6.12-1 documentation, dassault systems. Providence, RI, USA: Simulia Corporation; 2012.
[44] Zhang M, Jivkov AP. Micromechanical modelling of deformation and fracture of hydrating cement paste using X-ray computed tomography characterisation. Compos B Eng 2016;88:64–72.
[45] Farina I, Fabbrocino F, Carpentieri G, Modano M, Amendola A, Goodall R, et al. On the reinforcement of cement mortars through 3D printed polymeric and metallic fibers. Compos B Eng 2016;90:76–85.
[46] Torquato S. Random heterogeneous materials: microstructure and macroscopic properties. New York: Springer-Verlag; 2002.
[47] Bailakanavar MR. Space-time multiscale-multiphysics homogenization methods for heterogeneous materials PhD Thesis Columbia University; 2013.
[48] Scrivener KL. Skalny J, editor. The microstructure of concrete. Material science of concrete. Westerville (OH): American Ceramic Society; 1989. p. 127–62.
[49] Scrivener KL, Crumbie AK, Laugesen P. The interfacial transition zone between cement paste and aggregate in concrete. Interface Sci 2004;12:411–21.
[50] Bentz DP, Garboczi EJ, Stutzman PE. Maso JC, editor. Computer modeling of the

interfacial transition zone in concrete. Interfaces in cementitious composites. London, UK: E&FN Spon; 1993. p. 259–68 Part I, Chapter 6, Section 3.

[51] Scrivener KL. Alexander MG, Arliguie G, Ballivy G, Bentur A, Marchand J, editors. Characterization of the ITZ and its quantification by test methods. Engineering and transport properties of the interfacial transition zone in cementitious composites. France: RILEM Publications S.A.R.L.; 1999. p. 3–15. RILEM Report 20.

[52] Xotta G, Mazzucco G, Salomoni VA, Majorana CE, Willam KJ. Composite behavior of concrete materials under high temperatures. Int J Solid Struct 2015;64:86–99.

[53] Wang LM, Wu YF. Effect of corner radius on the performance of CFRP-confined square concrete columns: Test. Eng Struct 2008;30(2):493–505.

[54] Xiao Y, Wu H. Compressive behavior of concrete con ned by carbon fiber composite jackets. J Mater Civ Eng 2000;12(2):139–46.

[55] Menetrey P, Willam KJ. Triaxial failure criterion for concrete and its generalization. ACI Struct J 1995;92(3):311–8.

[56] Mazars J, Pijaudier-Cabot G. Continuum damage theory application to concrete. J Eng Mech-ASCE 1989;115(2):345–65.

[57] Mazars J, Pijaudier-Cabot G. From damage to fracture mechanics and conversely: a combined approach. Int J Solid Struct 1996;33(20–22):3327–42.

[58] Pijaudier-Cabot G, Bazant ZP. Nonlocal damage theory. J Eng Mech-ASCE 1987;113:1512–33.

[59] Grassl P, Lundgren K, Gylltoft K. Concrete in compression: a plasticity theory with a novel hardening law. Int J Solid Struct 2002;39(20):5205–23.

[60] Cervenka J, Vassilis KP. Three dimensional combined fracture-plastic material model for concrete. Int J Plast 2008;24(12):2192–220.

[61] Tarantino AM. Equilibrium paths of a hyperelastic body under progressive damage. J Elasticity 2014;114:225–50.

[62] Lanzoni L, Tarantino AM. Damaged hyperelastic membranes. Int J Non Lin Mech 2014;60:9–22.

[63] Lanzoni L, Tarantino AM. Equilibrium configurations and stability of a damaged body under uniaxial tractions. J Appl Math Phys 2015;66(1):171–90.

[64] Lanzoni L, Tarantino AM. A simple nonlinear model to simulate the localized necking and neck propagation. Int J Non Lin Mech 2016;84:94–104.

[65] Grassl P, Jirasek M. Damage-plastic model for concrete failure. Int J Solid Struct 2006;43(22):7166–96.

[66] Mazzucco G, Xotta G, Pomaro B, Majorana CE, Faleschini F, Pellegrino C. Mesoscale modelling of concrete with recycled aggregates. 10th int conf on mechanics and physics of creep, shrinkage, and durability of concrete and concrete structures, september 21-23. Vienna, Austria. 2015.